Journal of Materials Chemistry A

Accepted Manuscript

ROYAL SOCIETY OF CHEMISTRY

www.rsc.org/materialsA

$CuNb_{1-x}Ta_xO_3$ ($x \leq 0.25$) Solid Solution: Impact of Ta(V) Substitution and Cu(I) Deficiency on its Structure, Photocatalytic, and Photoelectrochemical Properties

Brandon Zoellner,[a] Sean Stuart,[b] Ching-Chang Chung,[c] Daniel B. Dougherty,[b] Jacob Jones,[c] and Paul A. Maggard[a,*]

[a]*Department of Chemistry,* [b]*Department of Physics, and* [c]*Department of Materials Science and Engineering, North Carolina State University, Raleigh, NC 27695-8204, United States*

A. Abstract

Solid solutions of Cu(I)-containing oxide *p*-type semiconductors provide key opportunities to probe the fundamental relationships between chemical compositions and crystal structure, bandgap sizes, band energies, and photoelectrochemical properties. Members of the $CuNb_{1-x}Ta_xO_3$ ($0 < x \leq 0.25$) solid solution series have been synthesized via high temperature solid-state methods. The structure of $CuNbO_3$ was found to be Cu-deficient $Cu_{0.965}NbO_3$ after heating in air at 250 °C for 3 hours, i.e., under similar conditions as used to prepare it as polycrystalline films. Powder X-ray diffraction techniques confirmed the purity of each composition up to $x \leq 0.25$ and the lattice parameters were refined as the molar ratio of Nb(V) and Ta(V) was varied (a = 9.499 to 9.506 Å, b = 8.439 to 8.451 Å, c = 6.768 to 6.781 Å and β = 90.847 to 90.694°). An increase in the amount of Ta(V) yielded a small blue shifting of the bandgap size from ~1.89 eV to ~1.97 eV for $CuNb_{1-x}Ta_xO_3$ from x = 0 to 0.25. Polycrystalline films of each member of the $CuNb_{1-x}Ta_xO_3$ solid solution produced relatively comparable *p*-type photocurrents of up to -0.5 mA/cm^2, while the stability of the cathodic photocurrent also remained similar with the increasing Ta(V) content. Mott-Schottky analysis of $CuNb_{1-x}Ta_xO_3$ found that the conduction band edge of -1.5 (vs. SHE) provides a sufficient overpotential (~800 mV) to drive the reduction of water to hydrogen gas at the surface. The capability for the solid solutions to produce H_2 gas was confirmed through suspended particle photocatalysis. Further characterization of the $CuNb_{0.91}Ta_{0.09}O_3$ composition included scanning electron microscopy, X-

ray photoelectron spectroscopy, and thermogravimetric analyses. These data show that Cu(I) is oxidized to Cu(II) as $CuNb_{1-x}Ta_xO_3$ is heated in air. Thus, the formation of Cu(II) rich regions at the surface, together with the Ta(V) content, are found to play important roles in the stability and magnitude of the cathodic photocurrents produced under visible-light irradiation. Importantly, these results demonstrate that the solid solution compositions can be used in films for solar energy conversion, notwithstanding their inherent atomic disorder.

B. Introduction

Solid solutions have previously been investigated in the development of many new visible-light active photocatalysts, and which have made use of the shifting of the energetic positions of the valence and/or conduction band energies. For example, solid solution photocatalysts such as $(Ga_{1-x}Zn_x)(N_{1-x}O_x)$ and $ZnS\text{-}CuInS_2\text{-}AgInS_2$ have been intensely investigated because of their activities for total water splitting into hydrogen and oxygen under visible-light irradiation.[1–3] In recent studies by the Maggard research group, the solid solution $Li_{1-x}Cu_xNb_3O_8$ was shown to have a bandgap size of ~3.9eV to ~1.3 eV that decreased with an increasing amount of Cu(I) substitution. This was found to originate from the introduction of the filled $3d^{10}$ copper orbitals that yields a new higher-energy valence band. In another example, the $NaCu(Ta_{1-x}Nb_x)_4O_{11}$ solid solution was investigated in order to probe changes in the bandgap size with the increasing substitution of the lower-energy niobium 4*d*-orbitals.[4,5] The emphasis of these past investigations has been the changes in the bandgap sizes and photocatalytic activities when in the form of suspended powders. Relatively less attention has been paid to photoelectrochemical investigations of metal-oxide solid solutions in the form of polycrystalline films. Important questions to be answered about such films include how changes in the electronic band structure influences the band positioning with respect to the redox potentials for the water splitting half reactions, or as well, how it impacts the photocurrents produced under visible-light irradiation. The naïve expectation is that the atomic disorder present in a solid solution will act to lower the mobility of the photoexcited charge carriers and result in significantly decreased photocurrents. This effect was observed for $Sr_2Nb_xTa_{2-x}O_7$ as the niobium content was increased.[6] Conversely, research on the mixed-cation solid solutions of $Fe_2O_3\text{-}Nb_2O_5$ and $BiFeO_3\text{-}SrTiO_3$ concluded that the varying compositions led to a decreased resistivity and improved photoelectrochemical performance as .[7,8] The majority of solid solutions investigated

thus far have focused on decreasing the band gap by introducing new energy levels that are less positive than the valence band or more positive than the conduction band. However, the introduction of new energy states away from the band edges should be studied in order to further understand the effects of the atomic disorder in solid solutions. Some examples of solid solutions with higher conduction-band energy substitutions include $Ca_2Nb_{2-x}Ta_xO_7$,[9] $Sr_2KNb_{5-x}Ta_xO_{15}$,[10] and $SnNb_{2-x}Ta_xO_6$.[11] Reported herein is the first photoelectrochemical investigation of a mixed Nb/Ta solid solution in the form of *p*-type polycrystalline films, including photocurrents and band energy measurements as a function of composition.

The mixed-metal $CuNb_{1-x}Ta_xO_3$ solid solution was selected owing to the previously reported stable photocurrent response and visible-light band gap of ~1.95 eV for the parent *p*-type semiconductor $CuNbO_3$.[12] The band gap of $CuNbO_3$ is favorable because it is close to the ideal ~1.7-2.0 eV for maximum efficiency according to the estimated overpotentials in combination with the Shockley-Quiesser limit.[12] Solid solutions between Ta(V) and Nb(V) in non Cu(I)-containing mixed-metal oxides have demonstrated the impact of the metal cations on the local structural features,[13] dielectric constants,[14–16] band gaps,[4,5] and electronic and photocatalytic properties.[17–19] In the present study, the effects of heating $CuNbO_3$ in air on its composition, structure, and photoelectrochemical properties have been investigated. Additionally the $CuNb_{1-x}Ta_xO_3$ solid solution was investigated for the extent of possible Ta(V) substitution into the structure and the resulting effects of the mixed Nb(V)/Ta(V) composition upon its crystalline structure and photoelectrochemical properties.

C. Experimental Methods

i. Materials

The starting reagents were purchased and used without further purification, including Cu_2O (99.9%, Alfa Aesar), Nb_2O_5 (99.9985%, Alfa Aesar), and Ta_2O_5 (99.99%, Acros Organics). The electrolyte solution for the photoelectrochemical measurements was made by dissolving Na_2SO_4 (99.0%, Alfa Aesar) and NaOH (> 97%, Fisher Scientific) in deionized water.

ii. *Synthesis*

Reactions targeting members of the solid solution series with the compositions $CuNb_{1-x}Ta_xO_3$ ($0 < x \leq 0.25$) were performed using solid-state reaction methods. Stoichiometric amounts of Nb_2O_5, Ta_2O_5, and Cu_2O (with a 20% molar excess) were ground into a fine powder

with a mortar and pestle for 30 minutes. The homogeneous mixture was dried overnight at 80 °C and then sealed under vacuum (~50 mTorr) in a fused-silica ampoule. The ampoules were placed in an alumina crucible and heated in a box furnace. The samples were next heated to a temperature of 900 °C for 12 hours and held for 24-48 hours before cooling back to room temperature over a period of 12 hours. The resultant products were stirred in 0.5 M HCl to dissolve any unreacted Cu_2O, followed by repeated centrifugation in water until a neutral pH was measured for the supernatant. After washing, the final product for each of the solid solution compositions was observed to have a similar bright red color with yields of at least >95%.

iii. *Characterization Methods*

Each compound was characterized by powder X-ray diffraction (PXRD) techniques (INEL, Cu $K\alpha_1$ λ = 1.54056 Å, CPS120 detector). The experimental XRD for each powder was compared to the calculated $CuNbO_3$ diffraction pattern, as determined from the previously reported single crystal refinement data.[20] The experimental lattice parameters were refined in the program LATCON for each solid solution using a total of 27 peak positions (*hkl*) for $CuNbO_3$.[21] A listing of the main peak positions is given in Table S1 of the Supporting Information.

A structural Rietveld refinement was performed on a powder sample of $CuNbO_3$ that had been heated to 250 °C for 3 hours in air. The powder X-ray diffraction pattern was collected on a PANalytical Empyrean X-ray diffractometer equipped with a PIXcellD detector at room temperature over a range of $10 \geq 2\theta \geq 90°$ with a step size and count time of 0.013° 2θ and 94 sec/step, respectively. The Rietveld refinement was performed using the GSAS II software. The reported crystal structure of $CuNbO_3$ was used as the initial model for the refinement within the monoclinic space group C *2/m* (a = 9.525(1) Å, b = 8.459(2) Å, c = 6.793(1) Å, β = 90.9(2)°).[20,22] To begin the refinement, the Chebyschev background function with 10 terms was refined along with the scale factor. The unit cell and sample displacement were then refined for several cycles until convergence was reached. Next, the atomic positions were refined individually in the order of niobium, copper, and oxygen. Preferred orientation along the 110 plane was observed in the diffraction pattern due to texture in the powder from sample preparation. The preferred orientation was modeled with the March-Dollase function during the refinement.[23,24] Additionally, refinements to the isotropic microstrain as well as the domain size of the particles were performed to correct peak shape and intensity. The thermal parameter

values (U_{iso}) for Nb(V) and Cu(I) cations were refined with the four Nb(V) U_{iso} values constrained to each other while the two Cu(I) U_{iso} values were refined independent of each other. Finally, the fractional occupancies of the Cu(I) sites were refined. The atomic positions, U_{iso} values, and the copper fractional occupancies were refined in multiple cycles to reach a final convergence.

X-ray photoelectron spectroscopy was carried out in an ultra-high vacuum chamber (base pressure 5 x 10^{-10} T) with a Riber MAC2 electron spectrometer. A non-monochromatic excitation source (Mg K_α radiation (1253.6 eV)) was used. Energy resolutions of ~2 eV and ~1 eV were used for survey and detail scans, respectively. The spot size of the X-ray beam on the sample was ~2-3 mm. Powdered samples were placed onto fluorine-doped tin oxide (FTO) and attached to the sample holder in air before being loaded into the XPS chamber and evacuated. The commercial software CasaXPS was used to analyze the spectra.[25] Energy scales were calibrated by assigning adventitious carbon peaks at 284.5 eV. A JEOL JSM-6400F field-emission scanning electron microscope (FESEM) was used to characterize surface changes of $CuNb_{0.91}Ta_{0.09}O_3$ after synthesis, annealing, oxidation, as well as after solar irradiation under a -0.25 V applied bias vs. SCE in a photoelectrochemical cell (described below). Thermogravimetric analyses were performed on a Q50 TGA instrument. Selected samples of $CuNb_{1-x}Ta_xO_3$ were annealed under vacuum at 500 °C for 3 hours before ~8-12 mg of each powder was heated in atmosphere. The temperature and time were selected to match the same conditions as used to prepare the films. The change in mass for each experiment was recorded for the entire duration of the heating and cooling process. These data were processed using the Universal Analysis 2000 data analysis software to calculate the change in mass percent. UV-Vis diffuse reflectance spectra were recorded using a Shimadzu Spectrometer UV-3600 with an integration sphere in the wavelength range of 200-1200 nm. Individual samples were measured on a pressed $BaSO_4$ plate as the background.

iv. *Photoelectrochemical Measurements*

Polycrystalline films for each sample were prepared on fluorine-doped tin oxide (FTO, TEK-15) glass slides. The FTO glass slides were washed by sonication for 30 minutes in deionized water, ethanol, and then acetone for two cycles. Films of each powder sample were prepared by taping off a ~4 cm^2 or ~1 cm^2 square area on an FTO glass slide with two layers of

Scotch tape. Depending on the film area (either 4 cm^2 or 1 cm^2), either 60 mg or 20 mg of each sample was placed in a small vial with 7 drops of a mixture of a 25:5 mL ratio of tert-butanol:deionized-water solution. The vial was sonicated for 1 min before the slurry was drop-casted onto the exposed FTO slide. The polycrystalline film was pressed into a uniform flat film using the doctor-blade method. Each film was annealed at 500 ^oC under vacuum (~35 mTorr) for 3 hours, followed by heating in air at 250 ^oC for 3 hours.

Photoelectrochemical (PEC) measurements were carried out under a 250 W Xe arc lamp (Oriel company) with an AM 1.5 G filter and an irradiant power density of ~100 mW/cm^2 on films with an area of ~1 cm^2. A custom made Teflon cell housed the photoelectrode material on FTO glass for PEC experiments. The photochemical response was measured using a CH Instrument Model 620A Electrochemical Analyzer. Linear sweep voltammetry (LSV) was carried out over a potential range of 0.1 to -0.6 V vs. SCE at a scan rate of 0.025 V/s. Chronoamperometry measurements were taken for $CuNb_{1-x}Ta_xO_3$ films using a -0.25 V vs. SCE applied bias over a period of 5,000 seconds. A potentiostat from Princeton Applied Research, PARSTAT 2263 and PowerSuite software was used to perform Mott-Schottky experiments on films with an area of ~4 cm^2.

v. *Suspended Particle Photocatalysis*

Powder samples of $CuNbO_3$, $CuNb_{0.94}Ta_{0.06}O_3$, $CuNb_{0.85}Ta_{0.15}O_3$, and $CuNb_{0.75}Ta_{0.25}O_3$ were heated in air at 250 °C for 3 hours, similar to the film preparation conditions. A 1% by mass platinum cocatalyst was added to the surface of the particles using the photochemical deposition method in an aqueous solution of chloroplatinic acid ($H_2PtCl_6 \cdot H_2O$; Alfa Aesar, 99.95%) and methanol. After washing the powders in water and drying, ~50 mg of platinized sample was loaded into a quartz tube which was filled with a 20% by volume methanol solution in deionized water (pH ~ 6.7), as previously described.[26] Nitrogen gas was bubbled through the solution for 30 minutes in the dark before irradiation. An L-shaped tube was attached to the reaction vessel to collect any gas produced. A water plug was placed in the tube to prevent the gas from escaping and allowing for the volumetric determination of gas production. Suspended particle photocatalysis was performed under UV-Vis (λ > 230 nm) irradiation with a power density of 200 mW/cm^2. The collected gas was injected into a gas chromatograph (SRI Instruments model 8610C) equipped with a thermal conductivity detector (TCD) to characterize the gaseous products of the reaction.

D. Results and Discussion

i. *Structural Characterization*

The crystalline structure of $CuNbO_3$ (C *2/m*, $Z = 8$, $a = 9.488(2)$ Å, $b = 8.440(1)$ Å, $c = 6.763(2)$ Å, $\beta = 90.93(2)°$)) has been described previously.[20] Results of the powder XRD data closely match the calculated pattern generated from the literature, as shown in Figure 1. Polyhedral structural views are shown in Figure 2. Briefly, the structure consists of stepped NbO_3 layers that are each comprised of edge-shared NbO_6 octahedra that are condensed into 'Nb_4O_{16}' groups. Each 'Nb_4O_{16}' group is aligned roughly parallel to the [-101] plane and bridges via its corner oxygen atoms to neighboring 'Nb_4O_{16}' groups, forming staircase-like NbO_3 layers down the [010] axis, as shown in Figure 2. The Cu(I) cations are located between these layers and are linearly coordinated between two oxygen atoms from upper and lower 'Nb_4O_{16}' groups.

The similar ionic radii of Nb(V) and Ta(V) cations in octahedral environments (0.64 Å)[27] suggested the compatibility for the substitution of Ta(V) within the $CuNbO_3$ structure, i.e. $CuNb_{1-x}Ta_xO_3$. However, the previously reported $CuTaO_3$ is not isostructural to $CuNbO_3$ and forms only under high pressures; thus, a full solid solution is not expected.[28] As the Ta(V) content increases from $x = 0$ to $x = 0.25$, the diffraction peaks corresponding to the (220), (202), (130), and (022) Miller indices shift to lower 2θ values, as shown in Figure S1 in the Supporting Information. The peak positions stop shifting after the Ta(V) content is loaded at 28%, and then begins to shift back to higher 2θ values at 30% Ta(V). Impurities of Cu_2O and $Cu_5Ta_{11}O_{30}$ are observed at $x = 0.28$, Figure 1, showing that the composition limit of the solid solution is reached at a concentration below ~28% Ta(V). As the chemical composition of a solid solution changes, the lattice parameters of the unit cell follow a regular trend as described by Vegard's law.[29,30] Given the very similar ionic radii of Nb(V) and Ta(V) cations, the lattice constant changes are found to be relatively small, as shown in Figure 3. Refined lattice constants from the powder X-ray diffraction data show that as the amount of Ta(V) increases from $x = 0$ to $x = 0.25$, the *b* and *c* lattice parameters increase and the *β*-angle decreases in a regular fashion. At higher amounts of Ta ($x = 0.28$ and 0.30) these either trend back downwards (i.e., for the *b* and *c* lattice parameters) or upwards (i.e., for the β angle). The *a* lattice parameter shows relatively smaller and less regular trends, but is relatively constant until an abrupt shift at $x = 0.3$, as shown in the Supporting Information. The abrupt shift in this lattice-constant at $x = 0.3$ arises concomitant with the formation of the new $Cu_5(Ta_{1-x}Nb_x)_{11}O_{30}$ solid solution. Thus, the Ta-richest

composition of the solid solution occurs approximately at x = 0.25. For comparison, the previously reported $SrBi_2(Nb_{1-x}Ta_x)_2O_9$ solid solution exhibited no detectable changes in its lattice parameters with increasing Ta(V) content.[31]

ii. *Copper (I) Deficiency*

Previous research conducted by the Maggard group has investigated the impact of heating Cu(I) niobates and tantalates in air upon their crystalline structures, compositions, and photoelectrochemical properties. Transmission electron microscopy and scanning electron microscopy studies show that heating in air causes the extrusion of Cu(I) at their surfaces and oxidation to Cu(II) that results in the formation of surface islands of CuO and the Cu-deficient compositions $Cu_{1-x}Nb_3O_8$ and $Cu_{5-x}Ta_{11}O_{30}$.[32,33] While the photoelectrochemical properties of $CuNbO_3$ films have been reported previously after heating in air,[12] a similar investigation of the Cu(I) extrusion from its structure has not yet been reported.

To investigate the possibility and impact of Cu(I) extrusion from $CuNbO_3$, high-resolution powder X-ray diffraction Rietveld refinements and thermogravimetric analyses were performed on samples heated at 250 ^oC in air for 3 hours. At this temperature, the newly refined composition of $CuNbO_3$ is a Cu(I)-deficient $Cu_{0.965}NbO_3$ with no CuO detected in the PXRD, as shown in Figure 4 and Table S2. Along with the decrease in the copper occupancy, the refined unit cell parameters contract. As the copper content within the metal oxide decreases, the lattice parameters and bond distances shift in compensation, as listed in Table 1. All three dimensions of the unit cell contract, with the largest changes observed in the c lattice parameter (Δa = -0.06 %, Δb = -0.098%, and Δc = -0.18%). The compression of the unit cell causes a minor increase in the β angle from 90.930 to 90.936°. Other structural consequences of the copper deficiency include the changes within the O2-Cu1-O2 and O3-Cu2-O4 bonds connecting the two layers of the 'Nb_4O_{16}' clusters. A full comparison of bond distances to those in the original structure is given in Table 1, and the displacements of the cations is illustrated in the insert of Figure 4. The distance between O2 and Cu1 decreases by ~0.066 Å, while the distances between O3/O4 and Cu2 increase by ~0.136 and ~0.002 Å, respectively. Although the bond distances counteract each other, the O-Cu-O angles become slightly more linear. The O2-Cu1-O2 angle increases slightly from 177.48° to 178.24° while the O3-Cu2-O4 angle shifts from 175.48° to 177.32°. Within the 'Nb_4O_{16}' clusters, the Nb(V) cations displace closer together towards the center of the cluster. The changes for all bond distances are predominantly determined by shifts in the oxygen

positions, i.e., the positions of the metal cations within the crystal structure remain largely unchanged while the oxygen positions are displaced. The largest change among the interatomic distances is observed between O3 and Nb2, which decreases by ~0.58 Å as the O3 atom shifts away from Cu2 and towards Nb2. The bond distance changes between Nb1/Nb2 and the coordinating oxygens (O2, O3, and O4) are the largest due to their connectivity with copper. As the O2-Cu1-O2 bond angle becomes more linear, the O2 atoms displace away from Nb2. Similarly, as the O3-Cu2-O4 bonds straighten, the distance between Nb2 and O3 decreases while the Nb2-O4 distance increases. The Nb1/Nb2-O1 distances are not altered as much as this bonding network comprises the corner sharing links between the NbO_6 octahedra and has no connectivity with copper.

Thermogravimetric analyses (TGA) were performed on the members of the $CuNb_{1-x}Ta_xO_3$ solid solution at 250 ^oC in air in order to quantify the amount of oxygen gained (i.e., via surface Cu oxidation) under similar conditions as used for their film preparation, as described below. As the compounds were heated in air, the Cu(I) cations react at the surfaces according to the following chemical reaction.

$$CuMO_3 + \tfrac{1}{2}\, x\, O_2 \rightarrow x\, CuO + Cu_{1-x}MO_3 \quad (M = \text{mixed Nb/Ta})$$

As shown in Figure S3 and listed in Table 2, the solid solution compositions with x = 0.09 and 0.15 exhibited the largest weight gains, corresponding to a calculated Cu(I)-deficiency of ~2.6%. Smaller weight gains were observed for the other three compositions, yielding Cu(I)-deficiencies of ~1.5-1.6%. A comparison to the copper deficiency obtained from the Rietveld refinement, at ~3.5%, is slightly larger but gives a reasonable comparison between these two different techniques. These small differences in the calculated copper deficiency appears to stem from changes in sample preparation and has no major impact on the photoelectrochemistry described below. Thermogravimetric analysis allows for a rough comparison of copper extrusion and reactivity to form CuO on different samples. Related research on Cu_2O,[34–36] $CuWO_4$,[37] $CuBiO_4$,[38] $Cu_5Ta_{11}O_{30}$,[33] and Cu_3VO_4,[39] has shown that the deposition of CuO onto the surfaces of the *p*-type films can enhance and stabilize their cathodic photocurrents owing to the formation of type-II band offsets.

iii. *Photoelectrochemical Measurements*

The prior photoelectrochemical (PEC) investigation on polycrystalline films of *p*-type $CuNbO_3$ shows that this phase can yield photocurrents of up to ~0.1 mA/cm^2 under visible-light

irradiation.[12] This prior study utilized a light source with an irradiant power density many times larger than one sun. As described above, heating Cu(I) based niobates and tantalates in air produces copper-deficient compositions. The extent of copper deficiency, as well as the amount of CuO islands, increases the photocurrent produced by the semiconductor when irradiated by visible light. Prior research on Cu(I)-niobates and Cu(I)-tantalates, e.g., $CuNb_3O_8$ and $Cu_5Ta_{11}O_{30}$, have shown that their polycrystalline films exhibit significant cathodic photocurrents after heating in air at temperatures from 250 ^oC to 550 ^oC. [40,41] This is consistent with the several reports of CuO at the surface of Cu(I) oxides, especially Cu_2O. Initial PEC experiments on films of $CuNbO_3$ were conducted in air at various temperatures in order to find the film preparation conditions that yield the highest photocurrents, but without leading to significant decomposition of $CuNbO_3$. As shown in Figure 5, cathodic photocurrents were produced by the $Cu_{1-x}NbO_3$ electrode films after heating in air from 250 to 350 °C for 3 hours. Powder X-ray diffraction of the $Cu_{1-x}NbO_3$ films, shown in Figure S4, shows that CuO was produced on the films after heating to 350 °C and higher temperatures. Further heating of $Cu_{1-x}NbO_3$ to 400 °C causes the phase to begin to decompose. As the temperature increases past 400 °C, the peak intensity for the (220) plane decreases while peaks consistent with CuO continue to grow in intensity. Continuing to 550 °C, the (220) peak for $CuNbO_3$ is no longer observed, but CuO, $CuNb_2O_6$, and an unidentified phase are found. The decomposition of $Cu_{1-x}NbO_3$ eventually causes the photocurrent to diminish after heating to 500 °C. Thus, the cathodic photocurrents are found to increase with the amount of Cu(I) oxidation and extrusion at the surfaces, but prior to its complete decomposition.

These $Cu_{1-x}NbO_3$ films were next investigated for the impact of Ta(V) substitution on their photoelectrochemical properties. For the $CuNb_{1-x}Ta_xO_3$ solid solutions, photoelectrochemical measurements were performed on films with x = 0, 0.03, 0.09, 0.15, and 0.22 with an applied bias of 0.1 V to -0.6 V vs. SCE under chopped visible-light irradiation using an AM 1.5 G light filter. Each film was heated to 250 °C to avoid major decomposition while still being able to produce appreciable photocurrents. As shown in Figure 6, cathodic photocurrents are produced which are indicative of a *p*-type electrode. Interestingly, these photocurrents were roughly the same (within a few hundredths of a milliamp) between each film. In other examples of Ta-substituted solid solutions, the results of gas production and or photocurrents were greatly influenced by the Ta/Nb ratio such as $SnNb_{2-x}Ta_xO_6$ and $NaNb_xTa_{1-}$

$_xO_3$.[11,42]. The dark current of each film remained close to zero until the applied potential reached approximately -0.5 V vs. SCE, showing that the photocurrent was produced as a result of photon absorption by the $CuNb_{1-x}Ta_xO_3$ solid solution. The maximum measured photocurrent of each film was approximately -0.5 mA/cm^2. The substitution of Ta(V) for Nb(V) cations did not result in decreased photocurrents as might be expected from the increasing amount of Nb/Ta disorder in the structure, and which also decreases the number of low energy acceptor levels in the conduction band. However, both the dark current and photocurrents were significantly enhanced compared to the previously reported results on $CuNbO_3$,[12] likely owing to the improved film preparation procedures described herein.

The cathodic photocurrents of the polycrystalline films were also measured as a function of time, as shown in Figure 7. The $CuNb_{1-x}Ta_xO_3$ films for x = 0, 0.03, 0.06, 0.09, 0.15, 0.20, and 0.25 were irradiated under a simulated solar spectrum with an external bias of -0.25 V vs. SCE for 5,000 seconds. Each film produced a photocurrent over the course of 5,000 seconds similar to what was observed during the linear sweep voltammetry. Across all percentages of Ta(V), an initial photocurrent of greater than 10 μA decayed the fastest during the first 200 seconds. These spikes were observed each time the light was turned on and off as a result of the instantaneous electron-hole separation, i.e., non-Faradaic current, within the space charge layer until equilibrium was reached, as well from the equilibration of the concentration gradient at the electrode surfaces.[42] While the photocurrents of each film decayed most rapidly for the first 1,000 seconds of light irradiation, the photocurrents began to stabilize from 1,000 to 2,000 seconds. By a time of ~5,000 seconds, the photocurrents of all films had become relatively stabilized, with a ~50% decrease from the initial responses. At 5,000 seconds, the cathodic photocurrents fall within a range of 1.5 μA. Electrochemical instability is a common problem facing many of Cu(I)-containing oxides in photoelectrochemical cells such as Cu_2O. The copper ions are easily reduced at the electrolyte interface which produces a layer of copper metal that acts as a blocking layer and greatly diminishes the performance of the cell. Research on enhancing the stability of the electrodes has focused on coating Cu(I) oxides with other materials to prevent this self-reduction without hindering the transfer of charges.[33–36,43–46] Hydrogen production could not be detected in our setup during irradiation of these films. This is likely due to the absence of an appropriate surface catalysis such as platinum.[47] However, suspended particle catalysis of $CuNbO_3$ with 1% by mass Pt catalysis readily produced H_2 in a solution of

water and methanol, as described below. The initial promising results of the $CuNb_{1-x}Ta_xO_3$ as a photoelectrode, illustrates the potential for efficient H_2 production under visible-light irradiation with the appropriate surface protection and the importance of CuO on the surfaces of Cu(I)-based oxides to facilitate charge separation.[34,35,39] The similar photocurrents of the solid solutions with increasing Ta percentage suggests that not all solid solutions are impacted the same way in terms of their photoelectrochemical properties.

iv. *Suspended particle photocatalysis*

Suspended particle photocatalysis measurements were used to compare the activities for photocatalytic hydrogen production of the solid solutions in an aqueous solution. When platinum is deposited onto the particles' surfaces it serves as a kinetic aid for electron transfer. A sacrificial reagent, such as methanol, prevents the oxidation of water as the rate-limiting step, which allows for only hydrogen and carbon dioxide to be produced as the photocatalytic products.

The series of solid solutions including $CuNbO_3$, $CuNb_{0.94}Ta_{0.06}O_3$, $CuNb_{0.85}Ta_{0.15}O_3$, and $CuNb_{0.75}Ta_{0.25}O_3$ with the same pretreatment of heating in air and platinum deposition were irradiated under UV-Vis irradiation with a power density of 200 mW/cm^2. While all compositions were active for producing hydrogen gas under these conditions (as confirmed by GC), there were clear differences in the total moles of hydrogen produced over a period of six hours of irradiation. The total moles of hydrogen gas produced continuously decreased as the tantalum content increased within the solid solution, as shown in Figure 8. The highest observed photocatalytic activity was for $CuNbO_3$ with a total amount of 142 μmol H_2/g. When 6% tantalum was substituted into the structure the hydrogen production decreased to 90 μmol H_2/g w. Increased substitution of tantalum at 15 and 25% yielded a total of 83 and 67 μmol/g of H_2 gas, respectively. The lower gas production with varying percentages of tantalum is observed in other UV-bandgap solid solutions between niobium and tantalum, as local sites within the crystal structure can distort and hinder charge transfer of the electrons and holes.[18] When no platinum was used, the amount of hydrogen also decreased to 47 μmol H_2/g for a sample of $CuNbO_3$ that was heated in air at 250 ^{o}C for 3 h. Further, while the photocurrents for the polycrystalline films were similar for each of the solid solutions, this occurs in the presence of an applied potential

where atomic disorder may have less of an effect as compared to the conditions for suspended-particle photocatalysis.

One similar aspect between each sample was the time over which the most of the hydrogen and carbon dioxide were produced. The largest amount of hydrogen was produced within the first one to two hours of irradiation, after which, the production of gas either ceased or continued regularly at a much slower rate. A similar decay in photocurrents was also observed in the chronoamperometry experiments when the solid solutions were studied in the form of films. The initial photocurrents would quickly decrease over a period of an hour until a smaller photocurrent became constant. The loss of reactivity was determined not to be from decomposition, as the X-ray diffraction patterns before and after remained identical, but rather arises from changes at the particles' surfaces (as described below).

iv. *Mott-Schottky Measurements*

To determine the effect of Ta(V) substitution on the band energies of $CuNb_{1-x}Ta_xO_3$, Mott-Schottky measurements were performed for each member of the $CuNb_{1-x}Ta_xO_3$ (x = 0, 0.03, 0.06, 0.09, 0.12) solid solution. A Mott–Schottky analysis involves the measurement of the capacitance of the electrode's surface when it is in contact with the electrolyte solution, as has been derived previously using the equation below: (C = capacitance (F) , ε = dielectric constant (F/m), ε_o = permittivity of free space (8.85×10^{-12} F/m), A= area of film (m^2), e = charge of electron (-1.60×10^{-19} C), N_A = acceptor density (cm^{-3}) as determined from the slope of the plot, V_o = potential (V vs. SHE), V_{fb} = flat-band potential (V vs. SHE), k = Boltzmann constant (8.617×10^{-5} eV/K), and T = temperature (K).[48] Additional information regarding the Mott-Schottky analysis is included in the Supporting Information.

$$\frac{1}{C^2} = \frac{-2}{\varepsilon\varepsilon_0 A^2 e N_A}\left(V_o - V_{fb} + \frac{\kappa_B T}{e}\right)$$

As shown in Figure 9, a plot of the inverse of the square of the capacitance against the applied potential gives a negative slope, confirming the *p*-type nature of the $CuNb_{1-x}Ta_xO_3$ solid solution films. Two frequencies, i.e., 25 Hz and 500 Hz (Figure S5), were used in the experiment to determine any frequency dependency that can arise for polycrystalline films.[49] The flat-band potential (V_{fb}) for each member of the solid solution was determined by extrapolating the linear portion of the Mott-Schottky plot to the *x*-axis to find V_o, as listed in Table 3. Using the equations $V_{fb} = V_o + kT/e$ and $E_v = V_{fb} + kT\ \ln(N_A/N_v)$,[48] the valence-band energies (E_v) were

calculated for all samples at the two different frequencies, as listed in Tables 3 and 4. The valence-band energies of each of the $CuNb_{1-x}Ta_xO_3$ films differed only by a few hundredths of a volt across the entire solid solution range from $x = 0$ to $x = 0.12$. This is consistent with the fact that the valence-band energies are primarily determined by the contributions from the Cu $3d^{10}$ orbitals, which are also apparently not significantly impacted by the substitution of Ta(V) for Nb(V) cations. Thus, the atomic contributions to the conduction band, i.e., the Nb(V) and Ta(V) cations, had little to no measurable effect on the valence band energies.

v. *Optical Properties*

The indirect band gap of polycrystalline $CuNbO_3$ films was previously reported to be ~1.95 eV, which enables a large fraction of the solar spectrum to be absorbed.[12] Previous research on various metal-oxide solid solutions has shown that the band gap can be either red- or blue-shifted, depending on the choice of the metal cations and their oxidation states.[4,5,50] The substitution of Nb(V) for Ta(V) has been shown to decrease the bandgap sizes of metal oxides, e.g., $Sr_2(Ta_{1-x}Nb_x)_2O_7$,[6,18] and $NaCu(Ta_{1-x}Nb_x)_4O_{11}$.[5] Conversely, the reverse substitution has been found to result in an increase in the bandgap sizes in tantalate compounds, e.g., $SnNb_{2-x}Ta_xO_6$,[11] $Ca_2Nb_2O_7$,[9] and $Sr_2KNb_{5-x}Ta_xO_{15}$.[10] UV-Vis diffuse reflectance data were taken in order to investigate the effect of Ta(V) substitution on the bandgap sizes and conduction band energies of the $CuNb_{1-x}Ta_xO_3$ solid solution. From the transformed Kubelka-Monk reflectance data, Tauc plots were used to evaluate the energies of the direct and indirect band gap transitions between $x = 0$ to $x = 0.22$, as shown in Figure 10.[51,52] As the amount of Ta(V) increases, there is a relatively minor blue-shift in both the direct and indirect band transitions by a few hundredths of an eV (1.89 to 1.97 eV (indirect) and 2.09 to 2.14 eV (direct)). These optical bandgap sizes can be added to the energetic position of the valence band i.e., as calculated from the Mott-Schottky data, in order to determine the energy of the conduction band for each of solid solution compositions. For all compositions, the calculated energy position for the conduction band is more negative than the reduction potential for hydrogen with an over potential of ~800 mV.

A shifting of the bandgap sizes and band energies, or lack thereof, in $CuNb_{1-x}Ta_xO_3$ can be understood via changes in the electronic structure across the range of solid solution compositions. The calculated densities-of-states and band structure for $CuNbO_3$ has been reported previously, finding that the filled copper $3d^{10}$ orbitals and empty niobium $4d^0$ compose the highest-energy valence band and lowest-energy conduction band states, resepectively.[12] As

the Ta(V)-content increases in the $CuNb_{1-x}Ta_xO_3$ solid solution, higher-energy Ta $5d^0$ orbitals are added above the conduction band edge. Conversely, the contribution of the Nb $4d^0$ orbitals decreases, resulting in a gradual decrease of the width in the conduction band. However, as the amount of Ta(V) does not exceed approximately 25%, the Nb-based conduction band remains relatively conserved. This is confirmed in the measurements of the optical bandgap sizes. A similar trend in the bandgap size was observed during the studies on the solid solutions of $Ca_2Nb_{2-x}Ta_xO_7$,[9] $HCa_2Nb_{3-x}Ta_xO_{10}$,[53] $Sr_2KNb_{5-x}Ta_xO_{15}$,[10] and $SnNb_{2-x}Ta_xO_6$[11] as the amount of Ta(V) is increased. A more significant blue-shifting of the bandgap size of $CuNb_{1-x}Ta_xO_3$ would be expected if the amount of Nb(V) could be decreased below the threshold for band formation in this structure, and eventually resulting in a new higher-energy conduction band formed by the Ta(V) cations.

vi. *Particle Morphologies and Surface Characterization*

Scanning electron microscopy (SEM) images were taken of $CuNb_{0.91}Ta_{0.09}O_3$ in order to evaluate the particle morphologies and sizes, shown in Figure 11. Solid-state reactions using the high-temperature ceramic method typically do not yield highly-defined particle shapes or well-faceted surface features. As shown in Figure 11 (a), the particles were predominantly micron-sized and exhibited a range of irregular particle morphologies and surface features. In addition, SEM images were taken on the $CuNb_{0.91}Ta_{0.09}O_3$ sample a) after annealing it at 500 °C for 3 hours in vacuum, b) heating in air at 250 °C for 3 hours, and c) after passing a photocurrent through its polycrystalline film for ~2,000 seconds under solar irradiation with a -0.25 V vs. SCE applied bias, as shown in Figure 11 (b-d). After heating the sample in air at 250 ^oC for 3 hours, the product showed the formation of nano-islands on the particles' surfaces. However, the low amounts of CuO formation did not result in a visually darker or black coloration of the film, as has been observed for other Cu(I)-niobates at higher temperatures.[33] After passing the photocurrent through the film of the $CuNb_{0.91}Ta_{0.09}O_3$ sample, the SEM images more clearly revealed that its surfaces were significantly covered with Cu-containing nano-islands.

Additional surface characterization of the $CuNb_{0.91}Ta_{0.09}O_3$ solid solution was performed using X-ray photoelectron spectroscopy after heating the powder in air at 250 ^oC for 3 hours and passing a photocurrent through its film for 5,000 seconds, as shown in Figure 12. Detailed scans from 925 - 975 eV for the sample heated in air exhibited peaks that correspond to the binding energies of the $2p_{3/2}$ and $2p_{1/2}$ core levels of Cu(II) cations. Thus, the XPS spectra of the

$CuNb_{0.91}Ta_{0.09}O_3$ sample heated in air revealed only Cu(II), and no Cu(I) could be detected at the surface. After a cathodic photocurrent was passed through the film for 5,000 seconds, the main peak for Cu $2p_{3/2}$ core level developed a small shoulder that can be assigned to Cu(I) or Cu(s) at the surfaces. This change in the spectra indicates the reduction of Cu(II) or Cu(I) to Cu(s) at the surfaces of the electrode, as is known to be the dominant degradation pathway for *p*-type films of Cu_2O as well. Similar observations of the reduction of CuO has been observed with CuO/Cu_2O electrodes.[54] The reduction of CuO at the surface thus also contributes to the decay of photocurrents during long term light exposure. Thus, the reduction of water to hydrogen is slowed as the surface Cu(II) cations are reduced. The majority of the spectrum remains unchanged, illustrating that most of the surface states of copper remain unchanged.

E. Conclusions

Members of the $CuNb_{1-x}Ta_xO_3$ ($0 < x \leq 0.25$) solid solution was synthesized using the solid-state reaction method and investigated to determine the impact that Nb/Ta solid solution compositions have on their photoelectrochemical properties. The incorporation of tantalum into $CuNbO_3$ results in increases in the *b* and *c* lattice parameters as well as a decreasing β angle of the unit cell, up to a limit of ~25% tantalum. Additional changes in the structure resulted from heating $CuNbO_3$ in air at 250 °C to produce a Cu-deficient composition i.e., $Cu_{1-x}NbO_3$. Results from Rietveld refinements show that the extrusion of Cu(I) causes a distortion in the coordination environment of copper between the niobate layers, causing the layers to contract and increasing the linearity of the copper-oxygen bonds. The Cu vacancies and CuO surface islands produced from heating $CuNbO_3$ in air lead to the significant photocurrents that are generated when $Cu_{1-x}NbO_3$ films are irradiated under visible light. As Nb(V) was substituted for Ta(V), the irradiated films produced nearly identical photocurrents across the full solid solution series. Only minor differences in the photoelectrochemical stabilities were observed while irradiating the polycrystalline films over a period of 5,000 seconds. Suspended particle photocatalysis shows that their photocatalytic activity to produce hydrogen gas decreases as the percentage of tantalum increases in the structure. From previously reported electronic structure calculations, the conduction band was found to remain composed of niobium 4*d*-orbitals. The minor blue shifting in the bandgap size of ~1.95-2 eV shows that the tantalum substitution had

no significant impact the energy on the conduction band edge. Changes in the flat-band potentials were not significant and did not alter the energetic position of the highest-occupied valence band states. The surfaces of the particles were observed to change through SEM and XPS, as the polycrystalline films were heated in air and after PEC experiments. Heating the films in air produced a Cu(II) rich surface of CuO, some of which was then found to become reduced during PEC experiments with changes in the XPS. These results show that solid solution compositions with energy states introduced away from the conduction band edge can be used in the photocatalytic production of hydrogen in the form of polycrystalline films or suspended powders, but which require further research into the stabilization of their surfaces.

F. Acknowledgements

The authors acknowledge the use of the Analytical Instrumentation Facility at North Carolina State University, which is supported by the State of North Carolina and the National Science Foundation. Dr. Chuck Mooney is also acknowledged for SEM images of $CuNb_{0.91}Ta_{0.09}O_3$.

G. References

(1) Tsuji, I.; Kato, H.; Kudo, A. *Angew. Chem. Int. Ed. Engl.* **2005**, *44*, 3565–3568.

(2) Tsuji, I.; Kato, H.; Kobayashi, H.; Kudo, A. *J. Phys. Chem. B* **2005**, *109*, 7323–7329.

(3) Maeda, K.; Teramura, K.; Takata, T.; Hara, M.; Saito, N.; Toda, K.; Inoue, Y.; Kobayashi, H.; Domen, K. *J. Phys. Chem. B* **2005**, *109*, 20504–20510.

(4) Sahoo, P. P.; Maggard, P. A. *Inorg. Chem.* **2013**, *52*, 4443–4450.

(5) Palasyuk, O.; Maggard, P. A. *J. Solid State Chem.* **2012**, *191*, 263–270.

(6) Yoshino, M.; Kakihana, M. *Chem. Mater.* **2002**, *14*, 3369–3376.

(7) Aroutiounian, V. M.; Arakelyan, V. M.; Shahnazaryan, G. E.; Stepanyan, G. M.; Khachaturyan, E. A.; Wang, H.; Turner, J. A. *Sol. Energy* **2006**, *80*, 1098–1111.

(8) Cho, S.; Jang, J.; Zhang, W.; Suwardi, A.; Wang, H.; Wang, D.; Macmanus-Driscoll, J. L. *Chem. Mater.* **2015**, *27*, 6635–6641.

(9) Zhang, L.; Fu, H.; Zhang, C.; Zhu, Y. *J. Phys. Chem. C* **2008**, *112*, 3126–3133.

(10) Wang, P.; Schwertmann, L. *J. Mater. Chem. A* **2014**, *2*, 8815–8822.

(11) Lee, C. W.; Park, H. K.; Park, S.; Han, H. S.; Seo, S. W.; Song, H. J.; Shin, S.; Kim, D.-W.; Hong, K. S. *J. Mater. Chem. A* **2015**, *3*, 825–831.

(12) Joshi, U. A.; Palasyuk, A. M.; Maggard, P. A. *J. Phys. Chem. C* **2011**, *115*, 13534–13539.

(13) Janaswamy, S.; Murthy, G. S.; Dias, E. D.; Murthy, V. R. K. *Mater. Res. Bull.* **2008**, *43*, 655–664.

(14) Tzou, W. C.; Chen, Y. C.; Yang, C. F.; Cheng, C. M. *Mater. Res. Bull.* **2006**, *41*, 1357–1363.

(15) Duguey, S.; Lebourgeois, R.; Ganne, J. P.; Heintz, J. M. *J. Eur. Ceram. Soc.* **2007**, *27*, 1087–1091.

(16) Chen, X. M.; Hu, G. L.; Yang, J. S. *J. Eur. Ceram. Soc.* **2000**, *20*, 1257–1260.

(17) Sayama, K.; Arakawa, H.; Domen, K. *Catal. Today* **1996**, *28*, 175–182.

(18) Kato, H.; Kudo, A. *J. Photochem. Photobiol. A Chem.* **2001**, *145*, 129–133.

(19) Zou, Z.; Ye, J.; Sayama, K.; Arakawa, H. *Chem. Phys. Lett.* **2001**, *343*, 303–308.

(20) Marinder, B. O.; Wahlstrom, E. *Chem. Scr.* **1984**, 157–160.

(21) Schwarzenbach, D. LATCON, 1975.

(22) Toby, B. H.; Von Dreele, R. B. *J. Appl. Cryst.* **2013**, *46*, 544–549.

(23) March, A. *Z. Krist.* **1932**, *81*, 285–297.

(24) Dollase, W. A. *J. Appl. Crystallogr.* **1986**, *19*, 267–272.

(25) Fairley, N. CasaXPS, 2011.

(26) Boltersdorf, J.; Maggard, P. A. *ACS Catal.* **2013**, *3*, 2547–2555.

(27) Shannon, R. D. *Acta Cryst* **1976**, *A32*, 751–767.

(28) Sleight A.W.; Prewitt, C. T. *Mat. Res. Bull* **1970**, *5*, 1–5.

(29) Vegard, L. *Zeitschrift für Phys.* **1921**, *5*, 17–26.

(30) Denton, A. R.; Ashcroft, N. W. *Phys. Rev. A* **1991**, *43*, 3161–3164.

(31) Sun, L.; Feng, C.; Chen, L.; Huang, S.; Wen, X. *Mater. Sci. Eng. B* **2006**, *135*, 60–64.

(32) King, N.; Sahoo, P. P.; Fuoco, L.; Stuart, S.; Dougherty, D.; Liu, Y.; Maggard, P. A. *Chem. Mater.* **2014**, *26*, 2095–2104.

(33) Sullivan, I.; Sahoo, P. P.; Fuoco, L.; Hewitt, A. S.; Stuart, S.; Dougherty, D.; Maggard, P. A. *Chem. Mater.* **2014**, *26*, 6711–6721.

(34) Zhang, Z.; Wang, P. *J. Mater. Chem.* **2012**, *22*, 2456.

(35) Wijesundera, R. P. *Semicond. Sci. Technol.* **2010**, *25*, 045015.

(36) Huang, Q.; Kang, F.; Liu, H.; Li, Q.; Xiao, X. *J. Mater. Chem. A* **2013**, *1*, 2418.

(37) H, C.; Leng, W.; Xu, Y. *J. Phys. Chem. C* **2014**, *118*, 9982–9989.

(38) Patil, R.; Kelkar, S.; Naphade, R.; Ogale, S. *J. Mater. Chem. A* **2014**, *2*, 3661–3668.

(39) Sahoo, P. P.; Zoellner, B.; Maggard, P. A. *J. Mater. Chem. A* **2015**, *3*, 4501–4509.

(40) Joshi, U.; Maggard, P. *J. Phys. Chem. Lett.* **2012**, *3*, 1577–1581.

(41) Fuoco, L.; Joshi, U. A.; Maggard, P. A. *J. Phys. Chem. C* **2012**, *116*, 10490–10497.

(42) Peter, L. In *Photoelectrochemical Water Splitting: Materials, Processes and Architectures*; Lewerenz, H. J.; Peter, L., Eds.; The Royal Society of Chemistry, 2013; pp. 19–51.

(43) Paracchino, A.; Laporte, V.; Sivula, K.; Grätzel, M.; Thimsen, E. *Nat. Mater.* **2011**, *10*, 456–461.

(44) Han, J.; Zong, X.; Zhou, X.; Li, C. *RSC Adv.* **2015**, *5*, 10790–10794.

(45) Lim, Y.-F.; Chua, C. S.; Lee, C. J. J.; Chi, D. *Phys. Chem. Chem. Phys.* **2014**, *16*, 25928–25934.

(46) Sahoo, P. P.; Zoellner, B.; Maggard, P. A. *J. Mater. Chem. A* **2015**, *ASAP*.

(47) Heller, A. *Science.* **1984**, *223*, 1141–1148.

(48) Gomes, W. P.; Cardon, F. *Prog. Surf. Sci.* **1982**, *12*, 155–215.

(49) Bondarenko, A. S.; Ragoisha, G. A. *J. Solid State Electrochem.* **2005**, *9*, 845–849.

(50) Palasyuk, O.; Palasyuk, A.; Maggard, P. A. *Inorg. Chem.* **2010**, *49*, 10571–10578.

(51) Morales, A.; Mora, E.; Pal, U. *Rev. Mex. Fis. S* **2007**, *53*, 18–22.

(52) Ebraheem, S.; El-Saied, A. *Mater. Sci. Appl.* **2013**, *4*, 324–329.

(53) Maeda, K.; Eguchi, M.; Oshima, T. *Angew. Chem. Int. Ed. Engl.* **2014**, 13164–13168.

(54) Won, D. H.; Choi, C. H.; Chung, J.; Woo, S. I. *Appl. Catal. B Environ.* **2014**, *158-159*, 217–223.

Tables

Table 1. Comparison of the interatomic distances in $CuNbO_3$ and in the refined Cu(I)-deficient $Cu_{0.965}NbO_3$ structure.

Bond	$CuNbO_3$ (Å)[20]	$Cu_{0.965}NbO_3$ (Å)	Difference (Å)
Cu1 – O2	1.878	1.812(11)	-0.066
Cu2 – O3	1.841	1.977(14)	0.136
Cu2 – O4	1.809	1.811(14)	0.002
Nb1 – O1	1.835	1.908(11)	0.073
Nb1 – O2	2.011	1.875(10)	-0.136
Nb1 – O3	2.133	2.079(7)	-0.054
Nb2 – O1	1.99	1.921(11)	-0.069
Nb2 – O2	2.032	2.213(9)	0.181
Nb2 – O3	2.77	2.190(14)	-0.58
Nb2 – O4	1.78	1.938(15)	0.158
Nb1 – Nb1	3.411	3.384	-0.027
Nb2 – Nb2	5.681	5.664	-0.017
Nb1 – Nb2	3.313	3.299	-0.014

Table 2. Calculated moles of CuO formed on the surface of $CuNb_{1-x}Ta_xO_3$ after heating at 250 °C for 3 hr and the corresponding Cu-deficient composition.

Initial Composition	Moles of CuO per Moles of Initial Sample	Composition After Heating in Air
$CuNbO_3$	0.016	$Cu_{0.984}NbO_3$
$CuNb_{0.97}Ta_{0.03}O_3$	0.015	$Cu_{0.985}Nb_{0.97}Ta_{0.03}O_3$
$CuNb_{0.91}Ta_{0.09}O_3$	0.026	$Cu_{0.974}Nb_{0.91}Ta_{0.09}O_3$
$CuNb_{0.85}Ta_{0.15}O_3$	0.026	$Cu_{0.974}Nb_{0.85}Ta_{0.15}O_3$
$CuNb_{0.78}Ta_{0.22}O_3$	0.016	$Cu_{0.984}Nb_{0.78}Ta_{0.22}O_3$

Table 3. Measured flat-band potentials vs. SHE at two different frequencies for each $CuNb_{1-x}Ta_xO_3$ film (pH = 12).

Composition	Flat-band (V) (25 Hz)	Flat-band (V) (500 Hz)
$CuNbO_3$	0.37	0.43
$CuNb_{0.97}Ta_{0.03}O_3$	0.37	0.42
$CuNb_{0.94}Ta_{0.06}O_3$	0.37	0.42
$CuNb_{0.91}Ta_{0.09}O_3$	0.35	0.39
$CuNb_{0.88}Ta_{0.12}O_3$	0.36	0.41

Table 4. Measured redox potential vs. SHE (@ pH = 12) of the valence-band edges for $CuNb_{1-x}Ta_xO_3$ films.

Composition	Valence band (V) (25 Hz)	Valence band (V) (500 Hz)
$CuNbO_3$	0.4182	0.4761
$CuNb_{0.97}Ta_{0.03}O_3$	0.4142	0.4594
$CuNb_{0.94}Ta_{0.06}O_3$	0.4191	0.4609
$CuNb_{0.91}Ta_{0.09}O_3$	0.3993	0.4311
$CuNb_{0.88}Ta_{0.12}O_3$	0.4072	0.4487

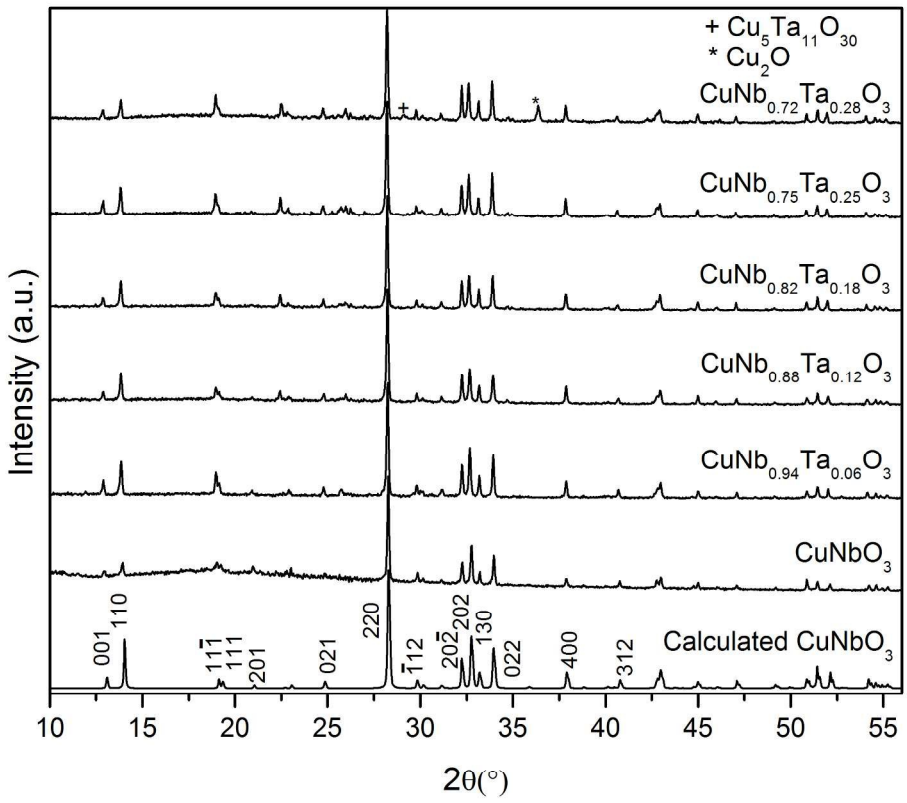

Figure 1. Experimental powder X-ray diffraction patterns of $CuNbO_3$ and $CuNb_{1-x}Ta_xO_3$ (x = 0.06, 0.12, 0.18, 0.25 and 0.28), with impurities marked as (*) $Cu_5Ta_{11}O_{30}$ and (+) Cu_2O and the calculated pattern of $CuNbO_3$ at the bottom.

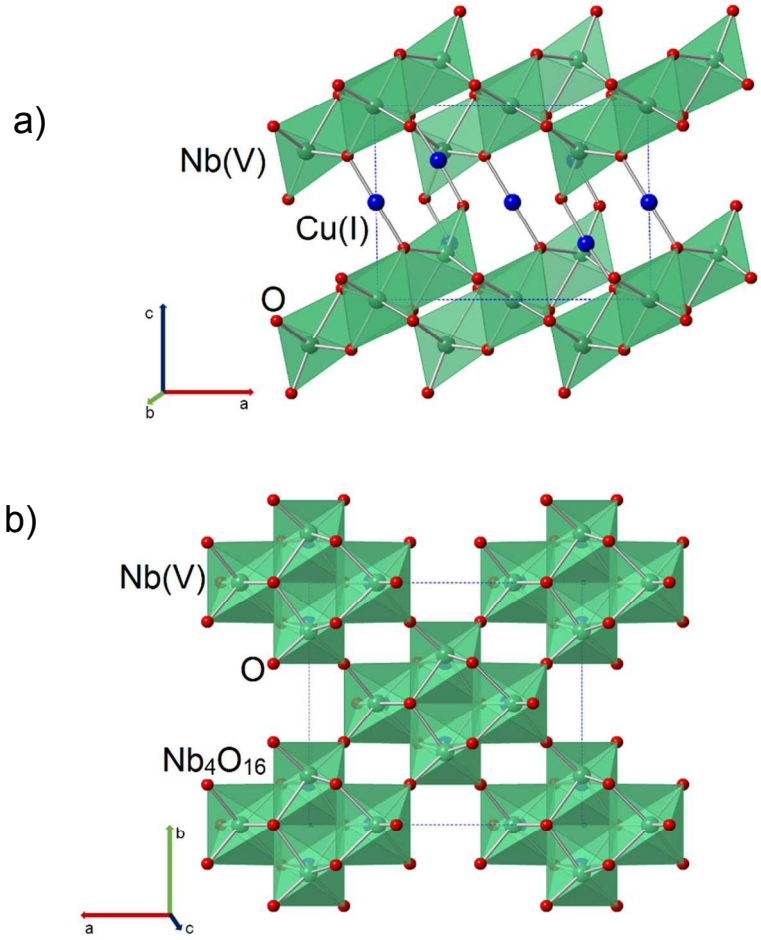

Figure 2. Polyhedral structural views of $CuNbO_3$ viewed down the [010] (a) and [001] (b) directions (Cu – blue, Nb –green, and O –red). The Cu(I) cations are linearly coordinated between two layers of corner-connected clusters of niobate octahedra.

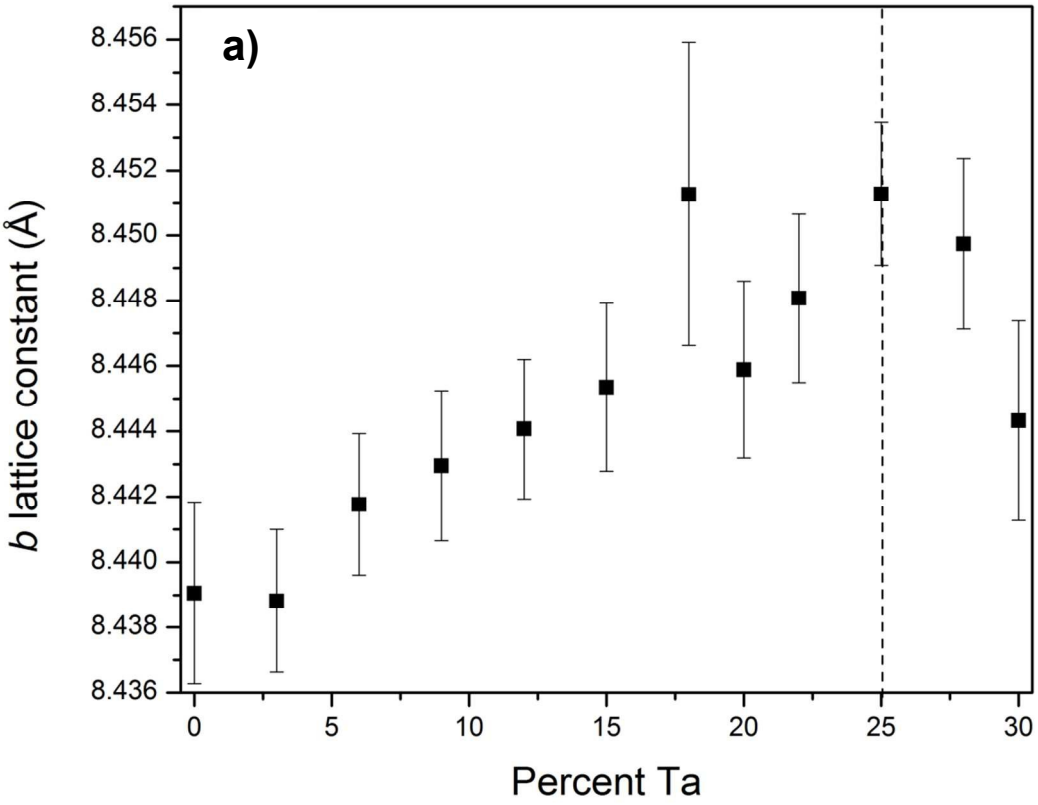

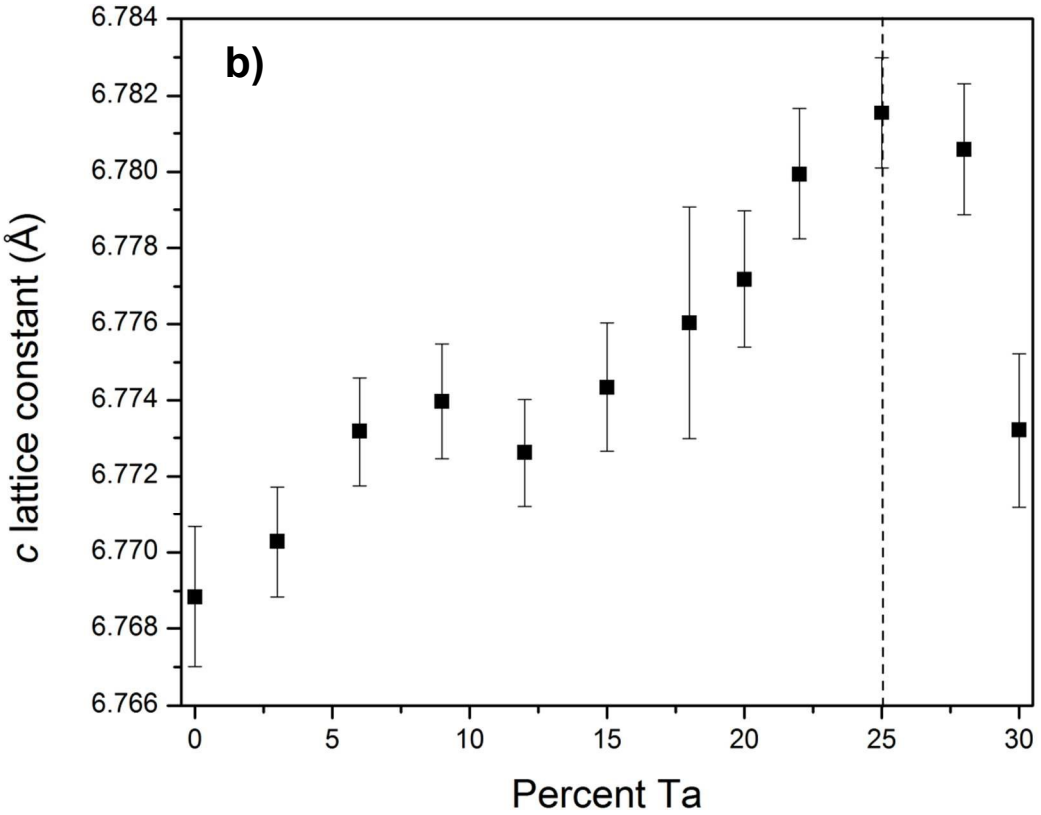

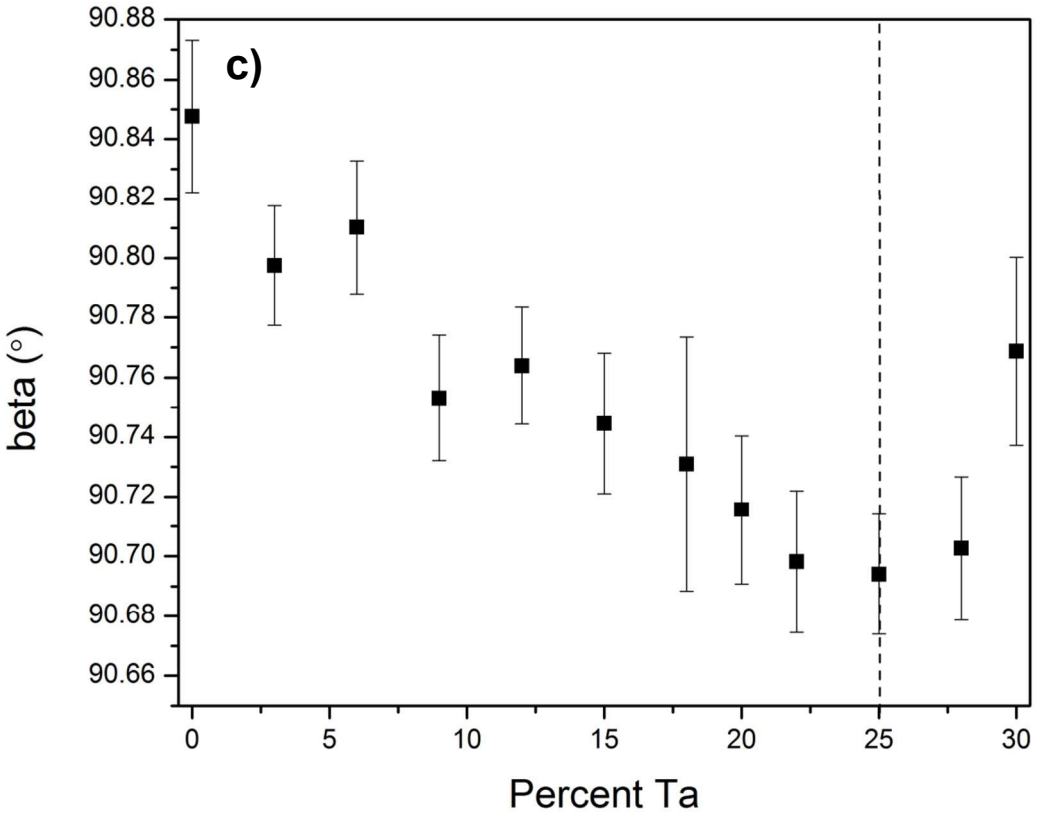

Figure 3. Refined lattice parameters of $CuNb_{1-x}Ta_xO_3$ ($0 \leq x \leq 0.30$) for the *b* lattice constant (a), *c* lattice constant (b), and beta angle (c), with error bars indicating the standard deviations.

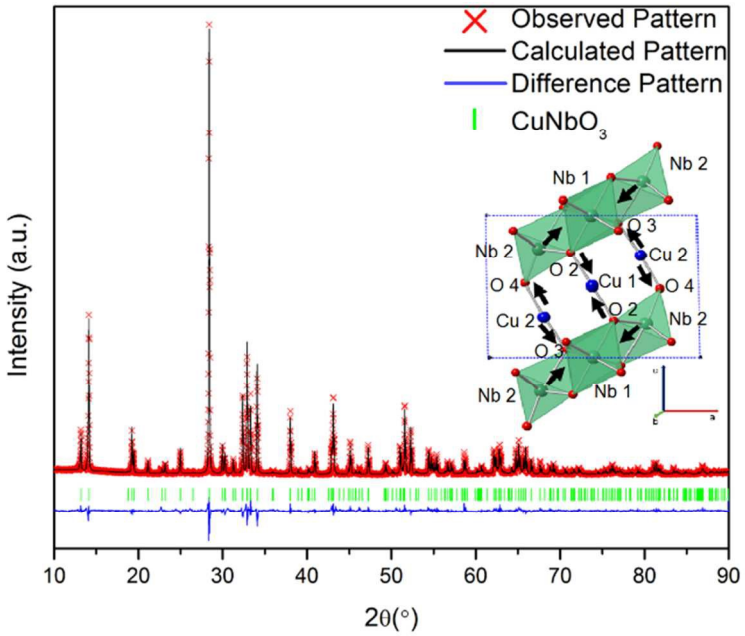

Figure 4. Rietveld refinement of the powder diffraction data of $Cu_{1-x}NbO_3$ heated in air at 250 °C for 3 hours. The red marks represent the observed diffraction pattern while the black line is the refine pattern representing the composition $Cu_{0.965}NbO_3$ (R_w = 3.762, GOF = 2.56). The inset shows a polyhedral view of $CuNbO_3$ unit cell with arrows indicating the directions of oxygen displacement that occurs after heating in air to become Cu(I) deficient.

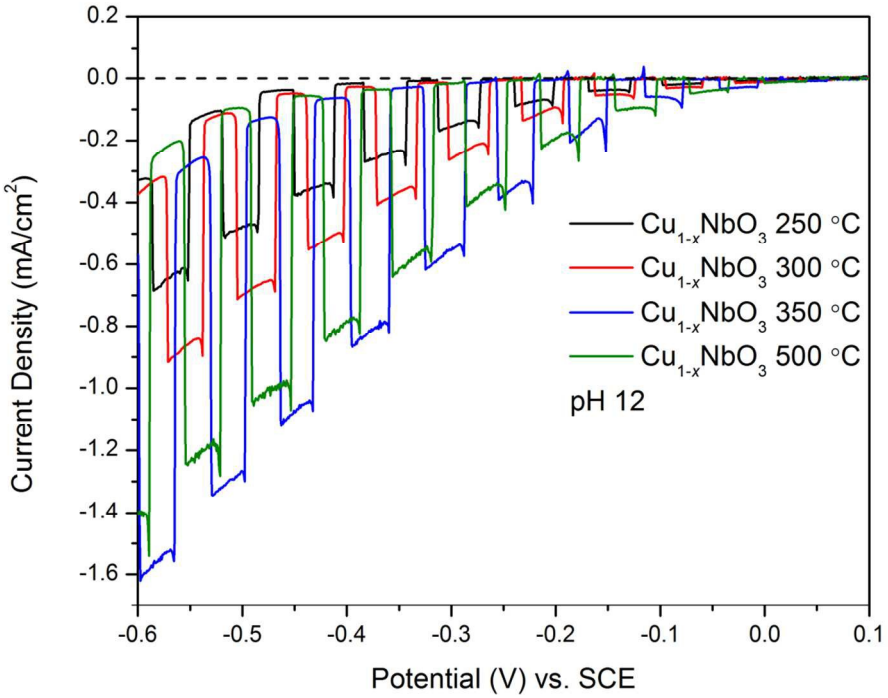

Figure 5. Linear sweep voltammetry of $Cu_{1-x}NbO_3$ films heated in air at temperatures of 250, 300, 350, and 500 °C for 3 hours.

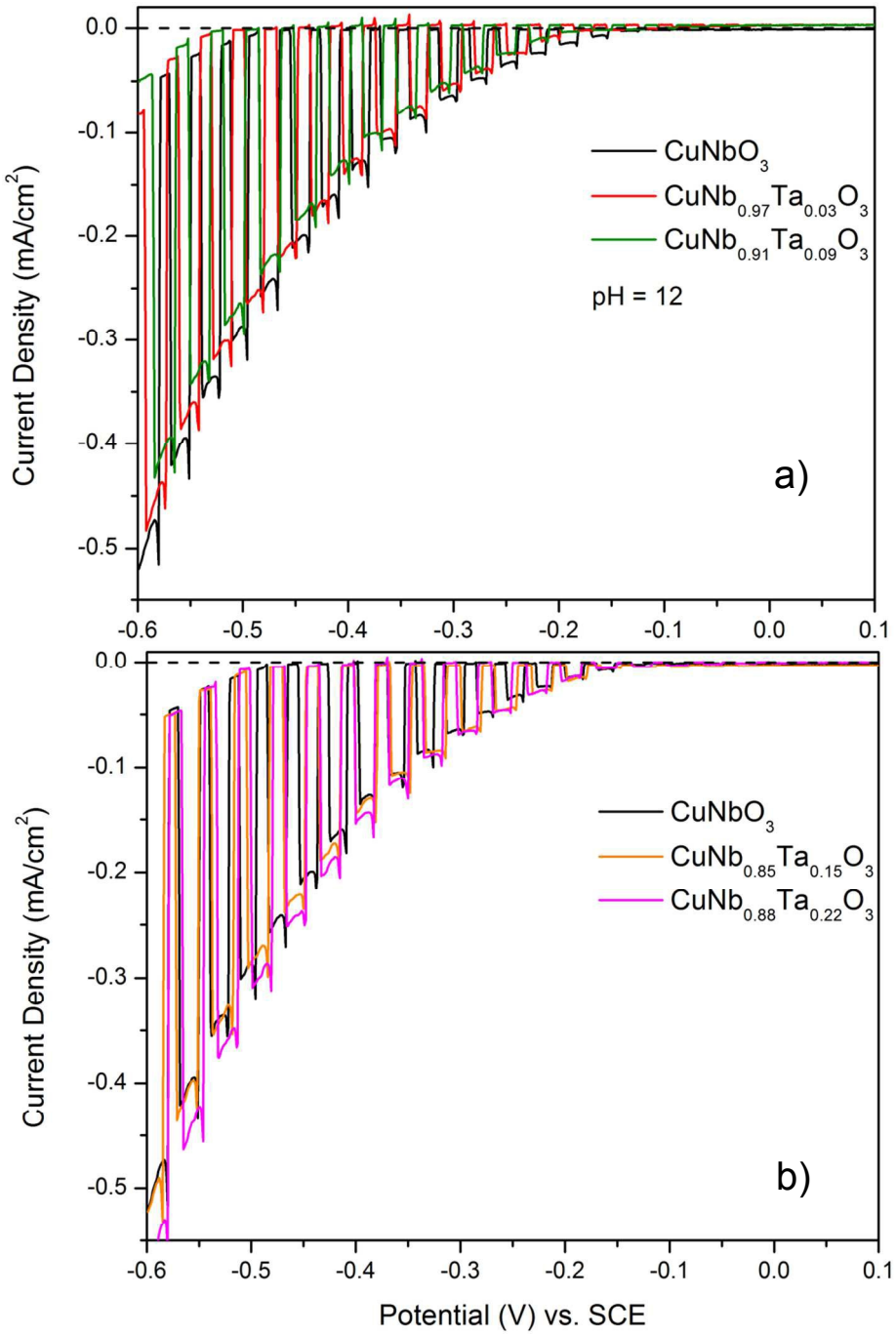

Figure 6. Linear sweep voltammetry measurements of $CuNb_{1-x}Ta_xO_3$ over the potential range of 0.1 to -0.6 V vs. SCE for 3 and 9% Ta (a), as well as 15 and 22% Ta (b).

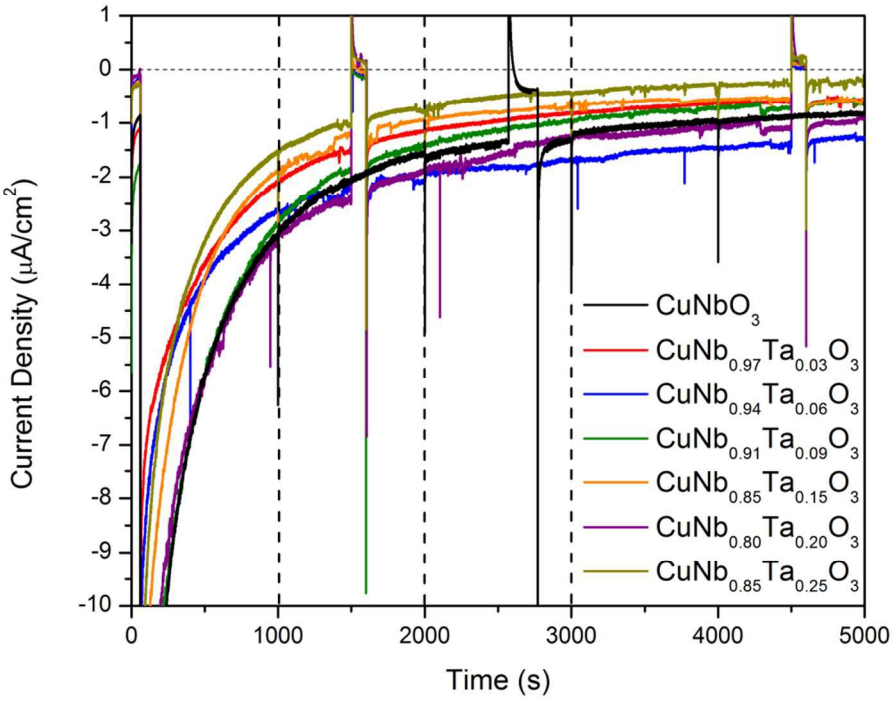

Figure 7. Chronoamperometry for a period of 5,000 s with an applied bias of -0.25 V vs. SCE for $CuNb_{1-x}Ta_xO_3$ (x = 0, 0.03, 0.09, 0.15, and 0.22).

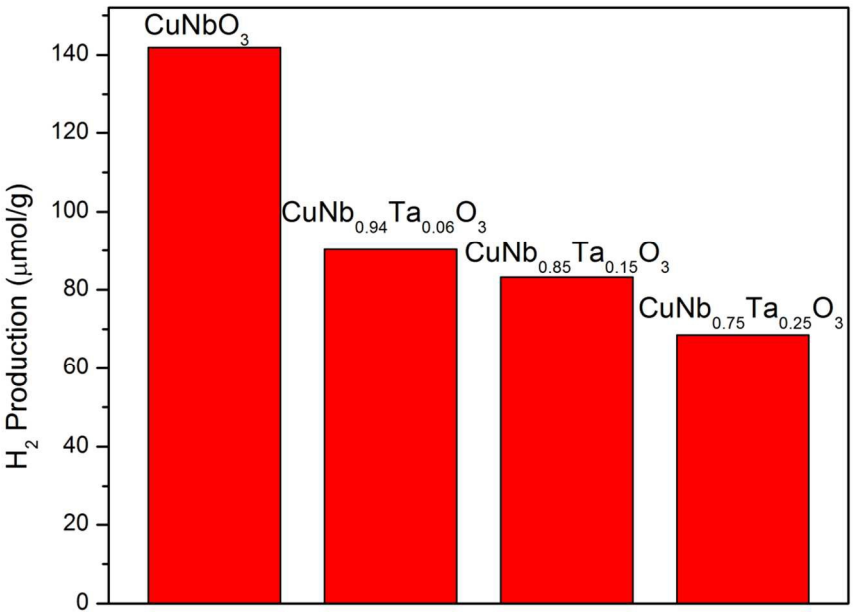

Figure 8. Total amount of H_2(g) produced per gram of $CuNb_{1-x}Ta_xO_3$ (x = 0, 0.06, 0.15, and 0.25) under UV-Vis irradiation at 200 mW/cm^2 for six hours.

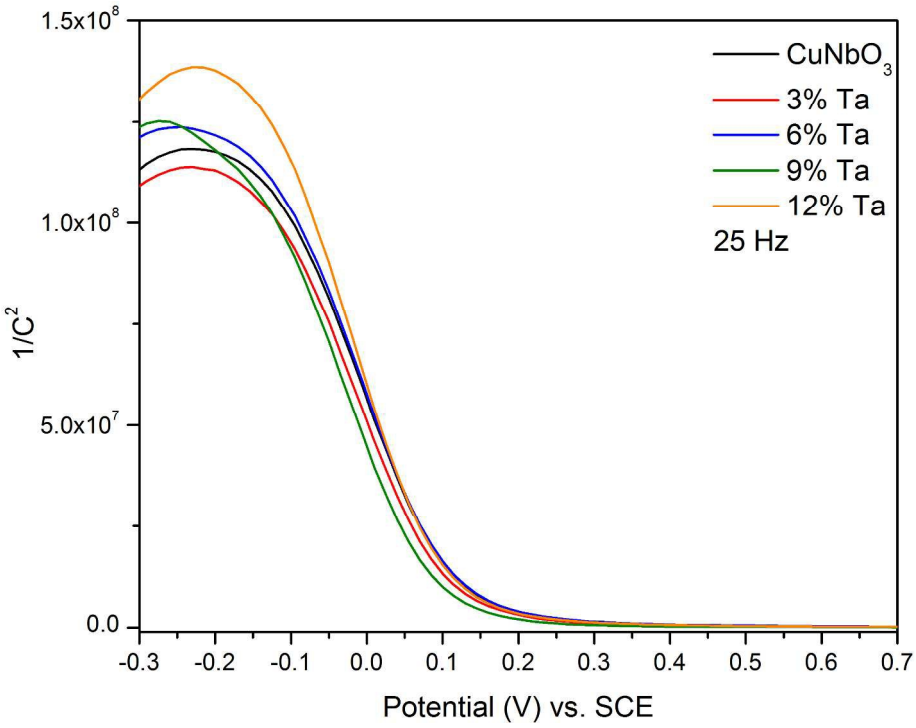

Figure 9. Mott-Schottky measurements of $CuNb_{1-x}Ta_xO_3$ (x = 0, 0.03, 0.06, 0.09, and 0.12) with a fixed AC frequency of 25 Hz.

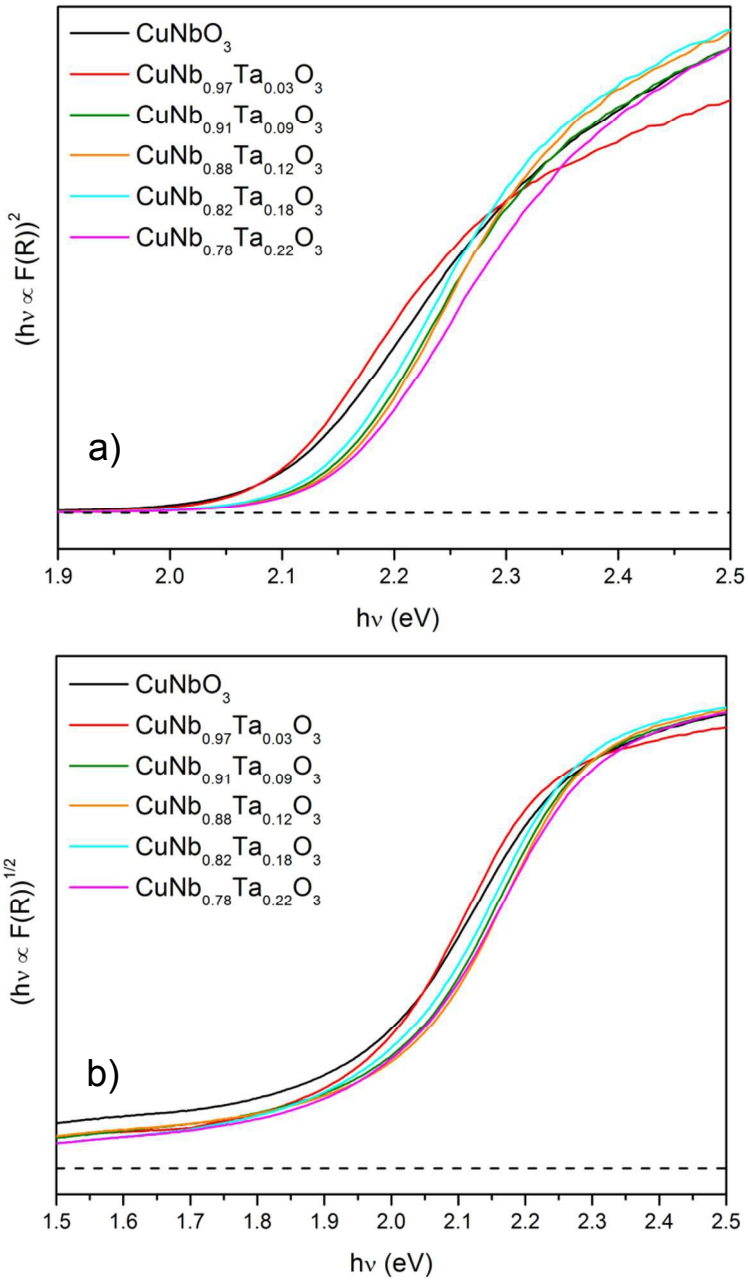

Figure 10. Tauc plots of direct (a) and indirect (b) bandgap transitions for $CuNb_{1-x}Ta_xO_3$ (x = 0, 0.03, 0.09, 0.12, 0.18, and 0.22).

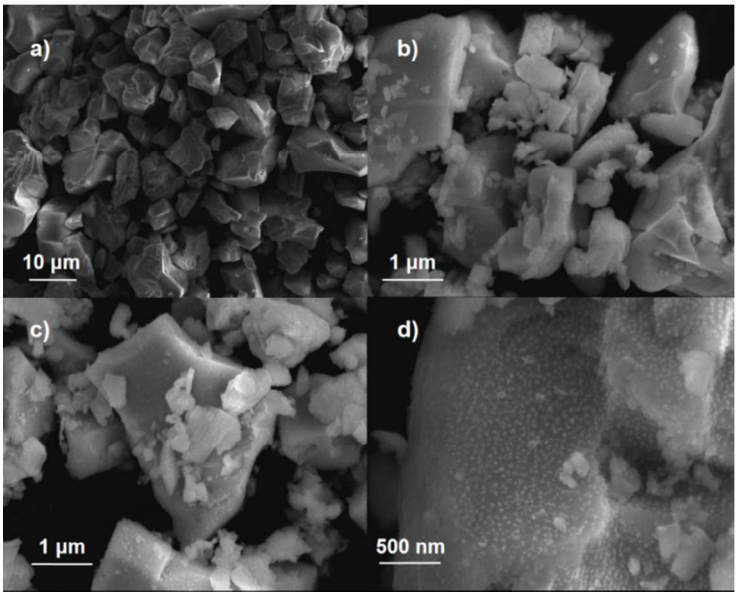

Figure 11. SEM images of $CuNb_{0.91}Ta_{0.09}O_3$ as synthesized (a), annealed under vacuum at 500 °C for 3 hrs (b), heated in air at 250 °C for 3 hrs (c), and after 2000 s under solar irradiation with a -0.25 V vs. SCE applied bias (d).

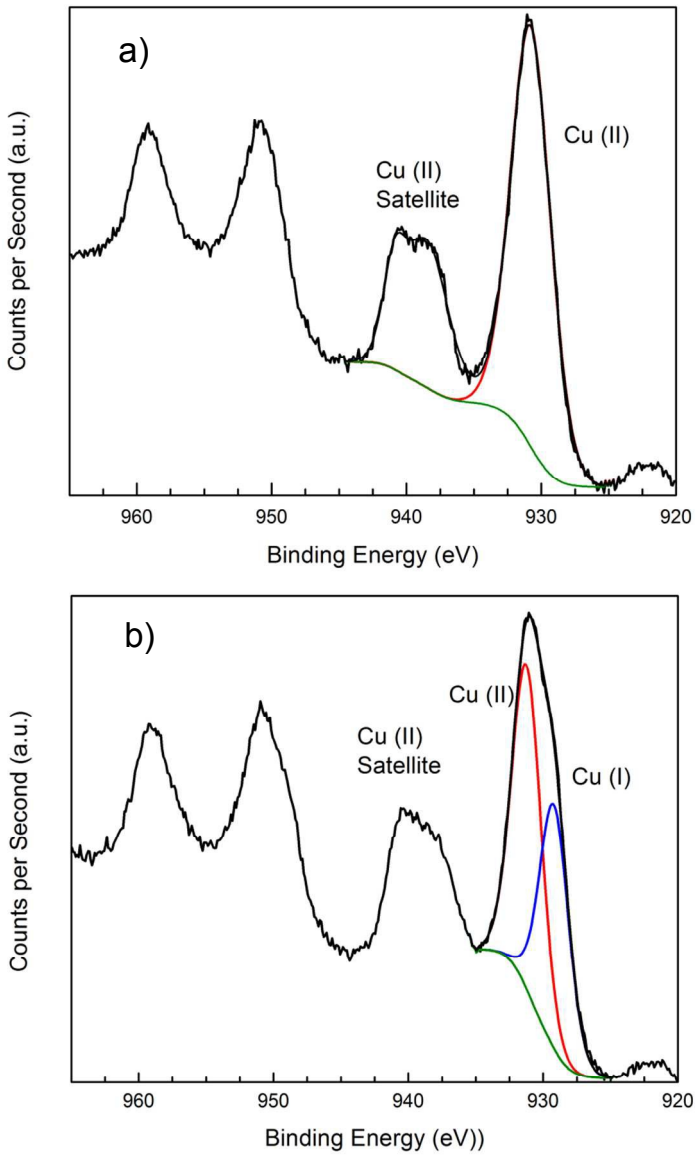

Figure 12: XPS data on films of $CuNb_{0.91}Ta_{0.09}O_3$ heated in air at 250 °C for 3 hrs (a) and $CuNb_{0.91}Ta_{0.09}O_3$ after being heated in air 250 °C for 3 hrs followed by irradiation under UV-Vis light for 5,000 s (b).

Table of Contents Image:

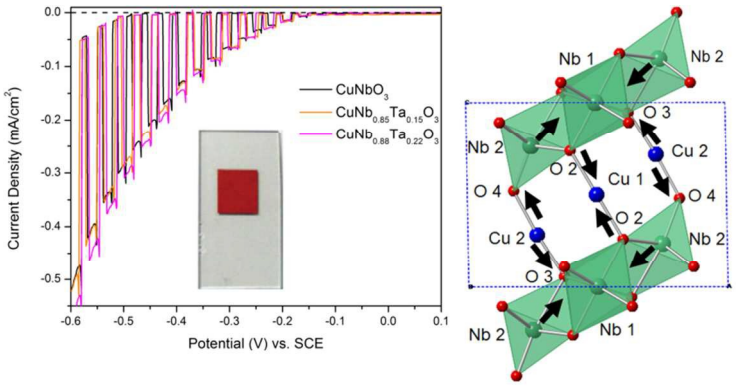

Table of Contents Caption: Investigation of $CuNb_{1-x}Ta_xO_3$ has led to new insights on the visible-light photocurrents and photocatalytic activities of solid solutions.